Physical Properties of Epitaxial $SrMnO_{2.5-\delta}F_{\gamma}$ Oxyfluoride Films

Jiayi Wang[1], Yongjin Shin[2], Nicolas Gauquelin[3], Yizhou Yang[1], Christopher Lee[1], Daen Jannis[3], Johan Verbeeck[3], James M. Rondinelli[2], Steven J. May[1]

[1] Department of Materials Science and Engineering, Drexel University, Philadelphia, Pennsylvania 19104, USA
[2] Department of Materials Science and Engineering, Northwestern University, Evanston, Illinois 60208, USA
[3] EMAT, University of Antwerp - Groenenborgerlaan 171, 2020 Antwerp, Belgium

E-mail: smay@drexel.edu

Received xxxxxx
Accepted for publication xxxxxx
Published xxxxxx

Abstract

Recently, topotactic fluorination has become an alternative way of doping epitaxial perovskite oxides through anion substitution to engineer their electronic properties instead of the more commonly used cation substitution. In this work, epitaxial oxyfluoride $SrMnO_{2.5-\delta}F_{\gamma}$ films were synthesized via topotactic fluorination of $SrMnO_{2.5}$ films using polytetrafluoroethylene (PTFE) as the fluorine source. Oxidized $SrMnO_3$ films were also prepared for comparison with the fluorinated samples. The F content, probed by X-ray photoemission spectroscopy (XPS), was systematically controlled by adjusting fluorination conditions. Electronic transport measurements reveal that increased F content (up to $\gamma = 0.14$) systematically increases the electrical resistivity, despite the nominal electron-doping induced by F substitution for O in these films. In contrast, oxidized $SrMnO_3$ exhibits a decreased resistivity and conduction activation energy. A blue-shift of optical absorption features occurs with increasing F content. Density functional theory calculations indicate that F acts as a scattering center for electronic transport, controls the observed weak ferromagnetic behavior of the films, and reduces the inter-band optical transitions in the manganite films. These results stand in contrast to bulk electron-doped $La_{1-x}Ce_xMnO_3$, illustrating how aliovalent anionic substitutions can yield physical behavior distinct from *A*-site substituted perovskites with the same nominal *B*-site oxidation states.

Keywords: oxyfluorides, oxide heterostructure, topotactic, electronic properties

1. Introduction

The doped manganite perovskites, written as $R_{1-x}A_xMnO_3$ (*R* = rare-earth metals, *A* = alkali or alkaline-earth metals), have been of interest owing to their various functionalities including metal-insulator transitions (MITs), colossal magnetoresistance, and spin-driven ferroelectricity [1-5]. These behaviors are achieved in part by tailoring the Mn oxidation state via *A*-site heterovalent cation substitution. In $La_{1-x}Sr_xMnO_3$, the substitution of divalent alkaline-earth Sr^{2+} for trivalent rare-earth La^{3+} produces a hole by oxidizing the $Mn^{3+}(t_{2g}^3e_g^1)$ into the $Mn^{4+}(t_{2g}^3e_g^0)$ state

[6,7], which then undergoes a x (Sr^{2+} concentration) dependent MIT and exhibits colossal magnetoresistance effects near x = 0.3 [1,8]. In contrast to the Mn^{3+}/Mn^{4+} mixed valence in $R_{1-x}A_xMnO_3$ materials, there is very limited choice of tetravalent cations for A-site substitution to realize the electron-doped Mn^{2+}/Mn^{3+} mixed-valence state containing $Mn^{3+}(t_{2g}^3e_g^1)$ and $Mn^{2+}(t_{2g}^3e_g^2)$. So far, Ce^{4+}-doped $La_{1-x}Ce_xMnO_3$ has been the most studied electron-doped manganite, with previous reports of a ferromagnetic insulator to ferromagnetic metal transition and the colossal magnetoresistance effect [9-12]. The amount of Ce doping alters the transport properties of $La_{1-x}Ce_xMnO_3$ as well; the resistivity decreases with increasing Ce content [12]. A MIT is also observed in this system at values of x ranging from 0.125 to 0.3 [11,12]. This transition is strongly dependent on the oxygen stoichiometry as both oxygen deficiency and excess have been reported in these compounds [9]. However, due to the lack of other electron-doped manganites for comparison, it remains unclear if the behavior in $La_{1-x}Ce_xMnO_3$ should be viewed as representative for mixed Mn^{2+}/Mn^{3+} behavior in perovskites or if such systems might host more diverse electronic and magnetic properties.

The substitution of F^- for O^{2-} within the perovskite structure provides an alternative route to electron-doping from A-site alloying as well as a means to control the ionicity of the transition metal-anion bond [13]. Fluorine insertion into transition metal oxides gained attention during the discovery of superconductivity in copper oxyfluoride $Sr_2CuO_2F_{2+\delta}$ [14-17], and since then has been applied to other functional oxyfluoride materials including ferrites [18-21] cobaltites [22,23], and manganites [24,25]. The effect of fluorination on the electronic and structural properties is strongly dependent on the mechanism of F incorporation, which can occur through F/O substitution, F incorporation at O vacancy sites, and F insertion into interstitial sites, corresponding to either reduction or oxidation of a transition metal ion during fluorination [26]. In previous studies of manganite oxyfluorides, both oxidative and reductive F incorporation has been observed. It was reported that the fluorination of bulk $SrMnO_{2.5}$ powders to $Sr_2Mn_2O_{5-x}F_{1+x}$ resulted in the oxidation of Mn cations to a mixed Mn^{3+}/Mn^{4+} valence, which suggests F incorporation into O vacancies was the dominant mechanism [25]. Fluorination of epitaxial $La_{0.74}Sr_{0.26}MnO_{3-\delta}$ films was found to occur through a combination of F insertion of anion vacancies and substitution for O, resulting in a decrease of the Curie temperature [27]. Our recent study of fluorination mechanisms in epitaxial $SrMnO_{2.5}$ films revealed F substitution for O as the dominant means of fluorine incorporation. Following fluorination, an increase in Mn^{2+} concentration was observed via X-ray absorption spectroscopy (XAS), as well as a lattice expansion also consistent with reduction of the Mn B-site cations [28]. Therefore, reductive fluorination of $A$$MnO_{2.5}$ provides a means to access new electron-doped families of manganites, albeit with chemical and structural distinctions that could lead to differing physical properties from $La_{1-x}Ce_xMnO_3$ compounds. The first distinction is an increased average ionicity of the Mn-anion bonds in the oxyfluoride compared to the Mn-O bonds in oxide manganites. Structurally, $A$$MnO_{2.5-\gamma}F_\gamma$ lacks the three-dimensional MnO_6 network found in $A$$MnO_3$ perovskites and instead consists of either uniform $Mn(O,F)_5$ square pyramids (if anion vacancy-sites are ordered) or combinations of MnO_4 tetrahedra, $Mn(O,F)_5$ square pyramids, and $Mn(O,F)_6$ octahedra (if anion vacancy-sites are disordered).

Here, we present a study of the physical properties of $SrMnO_{2.5-\delta}F_\gamma$ epitaxial oxyfluoride films with systematically controlled F content realized via vapor transport fluorination using polytetrafluoroethylene (PTFE). For comparison, we also detail the physical properties of oxidized $SrMnO_3$ films. We find that F incorporation system expands the lattice monotonically, increases resistivity, and blue-shifts the optical absorption spectra, trends that are opposite to what is observed in the oxidized films. In contrast to $La_{1-x}Ce_xMnO_3$, we do not observe a metal-insulator transition or ferromagnetic behavior up to γ = 0.13. These results illustrate how electron-doped complex oxides realized via heterovalent anion substitution can exhibit behavior distinct from their electron-doped analogues achieved through A-site substitution.

2. Methods

Epitaxial $SrMnO_{2.5}$ films were grown with oxide molecular beam epitaxy (MBE) on 10 × 10 mm^2 $(LaAlO_3)_{0.3}(Sr_2TaAlO_6)_{0.7}$ (LSAT) substrates with (001)-orientation. The substrate heater was held at approximately 600°C during growth. Films were grown in a chamber pressure of 2.5 × 10^{-6} Torr in O_2. The cation composition was determined by X-ray photoemission spectroscopy (XPS), which was calibrated through comparison to Rutherford backscattering spectroscopy (RBS) measurements of $SrMnO_{2.5}$ films. The films were grown by co-

deposition of Sr and Mn with a ~30 s deposition time per unit cell followed by a 10 s pause after each unit cell. The total film thickness for samples used in this study is approximately 40 nm. In situ reflection high-energy electron diffraction (RHEED) was used to monitor the surface crystallinity during the deposition process. The as-grown 10 × 10 mm^2 $SrMnO_{2.5}$ films were cut into nine equal square pieces with a sectioning saw to eliminate growth-to-growth variability in understanding how fluorination and ozone-induced oxidization alter physical properties.

The fluorination reaction was carried out using the vapor transport process. The as-grown $SrMnO_{2.5}$ film was placed downstream of PTFE pellets in an alumina boat, separated by a barrier made of aluminum foil to prevent their physical contact. The whole alumina boat was wrapped over by aluminum foil with two small holes punctured on both ends to preserve the fluorine containing PTFE decomposition products near the sample [21,28]. The alumina boat was placed in the middle of a quartz tube and heated in a tube furnace at temperatures ranging from 200 to 250°C and for reaction times from 15 to 720 min under an Ar gas flow maintained at 0.25 L min^{-1}. To achieve oxidized $SrMnO_3$ films, an ozone anneal was employed in which the $SrMnO_{2.5}$ film was placed in the middle of a quartz tube and annealed in an O_3/O_2 dilute mixture at 150°C for 1 h.

The crystalline quality and lattice parameters were assessed with X-ray diffraction (XRD) and X-ray reflectivity (XRR) measurements using a Rigaku SmartLab diffractometer. XRD measurements were taken about the 0 0 2 Bragg reflection of the film. XRD and XRR data were simulated in GenX [29]. The elemental composition and binding energy were probed by XPS depth profiling with Ar^+ ions sputtered at an energy of 1 keV. The sputtering cycle was carried out until reaching the substrate. Optical absorption spectra were measured with a J.A. Woolam M-200U variable angle spectroscopic ellipsometer over the energy range of 1.25 to 5 eV using 5 incident angles from 65–75°. The resistivity measurements were performed in a van der Pauw geometry with silver paint contacts in a Quantum Design Physical Properties Measurement System; dc magnetometry was performed using the vibrating sample magnetometry option on the same instrument.

The quality of the films was further measured by scanning transmission electron microscopy (STEM) on an aberration-corrected Titan microscope operated at 300 kV. The cross-sectional specimen of the fluorinated and the oxygenated samples were prepared using a focused ion beam (FIB). Imaging was performed in high angle annular dark field mode with a 20 mrad convergence angle and a collection angle of 41–95 mrad. For quantitative measurements, the images presented in the paper are the result of averaging 20 images acquired with short acquisition time (0.5 μs $pixel^{-1}$ in the linear regime of the detector) aligned for drift and distortion correction as described elsewhere [30]. The structural parameters were extracted from the images using the Python library Atomap [31].

Density functional theory (DFT) calculations were performed to investigate the electronic structure of manganite oxides and oxyfluorides using the Vienna *ab initio* simulation package (VASP) [32,33]. The spin-polarized generalized gradient approximation (GGA) of Perdew-Burke-Ernzerof (PBE) with the plus Hubbard U correction [34] was utilized [35]. A $U = 3$ eV value was applied to the Mn 3*d* orbitals to account for electron-electron interactions. The projector-augmented wave (PAW) method [36] was used to treat the core and valence electrons using the following configurations, Sr ($4s^24p^65s^2$), Mn ($3p^64s^23d^6$), O($2s^22p^4$), and F($2s^22p^5$), with a kinetic energy cutoff of 550 eV for the plane wave basis set. To accommodate the ground state antiferromagnetic order, $\sqrt{2} \times \sqrt{2} \times 2$ and 1 × 1 × 2 supercells of the $SrMnO_3$ and $SrMnO_{2.5}$ structures were prepared. 8 × 8 × 6 and 8 × 4 × 6 Monkhorst-Pack grids [37] were used for *k*-space sampling of the $SrMnO_3$ and $SrMnO_{2.5}$ Brillouin zones, respectively, and the integrations were performed with the tetrahedron method. The cell volume and atomic positions were relaxed until the forces on each atom were less than 5 meVÅ^{-1} while preserving the orthorhombic lattice without biaxial constraints.

Fluorinated $SrMnO_{2.5-\delta}F_\gamma$ systems were simulated by building 2 × 1 × 2 supercell of $SrMnO_{2.5}$ where one and two F atoms substituting for oxygen atoms yields $\gamma = 0.0625$ and 0.125, respectively. The atomic structures used for DFT calculations are described in supplementary figure S6. The spin order was set to collinear *G*-type antiferromagnetic (AFM) order for $SrMnO_3$, and *E*-type spin order for the oxygen deficient systems ($SrMnO_{2.5}$) [38]. To reproduce the optical spectra at the DFT-level, we computed the frequency-dependent dielectric tensor for the manganites using the PAW methodology [39] with 500 bands, ignoring local-field and finite lifetime effects. Then optical spectra were calculated using the Kramers-Kronig relations [40,41]. Although the independent particle picture does not provide a precise

quantitative description of the optical response, we show below that the changes in optical properties for the different phases is well described, giving good agreement with experimental data.

3. Results

3.1. Composition and structure

The film composition was determined by XPS depth profiling before and after fluorination. The Sr 3*d*, Mn 2$p_{3/2}$, O 1*s*, and F 1*s* photoelectron peaks were obtained. The photoelectron peaks of each element were analyzed with CasaXPS to get the atomic concentration respectively. We quantify the F concentration (γ) by normalizing the measured F content by the average atomic percentage of Sr and Mn. The overall γ value for each sample is determined by averaging the F atomic percentages obtained over cycles 5 to 15 in the XPS depth profile. Figures 1(a) and (b) show the XPS depth profiles of an as-grown and a fluorinated film. The sputtering time is 1 min for each measurement cycle, which removed ~2.2 nm of material. After 17 cycles, the sputtered depth reaches the film/substrate interface. From the depth profile of the as-grown $SrMnO_{2.5}$ film shown in figure 1(a), the Sr/Mn stoichiometry is close to 1. Figure 1(b) shows the depth profile after fluorination with PTFE at 225 °C for 720 min. The F is incorporated uniformly into the film, indicating that these reaction conditions allow sufficient time for the F to diffuse throughout the film. When sputtered into the LSAT substrate, which is between 20 to 27 sputtering cycles as shown in figure 1(b), the average F concentration is 0.88±0.7 % of the anion composition. Analysis from a second LSAT substrate yielded a F composition of 0.22±0.80 % of the anion sites. Considering the uncertainty, the amount of F incorporated into the LSAT substrate is believed to be minimal. XPS depth profiles highlighting the LSAT substrate region are presented in figure S1.

In order to determine if the F content can be adjusted through the fluorination conditions, XPS was measured on numerous films fluorinated at different temperatures and for different times. The F concentration versus reaction temperature and time are plotted in figures 1(c) and (d), respectively. Figure 1(c) shows the F content resulting from fluorination at different temperatures for 30 min. The increase in F concentration with temperature is modest until the fluorination temperature reaches 245 °C. Although increasing the reaction temperature to 250 °C results in further F incorporation, the film pseudocubic 0 0 2 XRD peak is no longer present in the sample treated at 250 °C, which indicates the crystallinity of the film or potentially phase stability is lost at higher fluorination temperatures as shown in Supplemental figure S2. Figure 1(d) shows the influence of reaction time on the incorporation of F when as-grown films are fluorinated at 200 °C. The F content increases steadily with reaction time, and the film XRD peak is maintained after fluorinating for 720 min. Thus, control of reaction time proves to be a promising way to control the fluorination level while maintaining the film crystallinity.

Film quality and lattice parameters were investigated using XRD and XRR. Figure 2(a) presents XRD data from five samples, all of which were originally cut from a single 10 × 10 as-grown $SrMnO_{2.5}$ film. The as-grown film is represented by the red curve, overlapped with a representative simulation in black. The *c*-axis parameter of the as-grown $SrMnO_{2.5}$ epitaxial film on LSAT is found to be 3.791 Å via comparison of the measured data with simulation. For the three fluorinated $SrMnO_{2.5-\delta}F_{\gamma}$ films in figure 2(a), the fluorination temperature was held at 200 °C for 60, 240, and 480 min, yielding γ = 0.04, 0.05, and 0.08, respectively, as labeled in the figure. We observe that the F content increases with longer fluorination time, consistent with the same trend reported in figure 1(d). The *c*-axis parameter also expands as the F content is increased, a trend shown in figure 2(b) for a variety of samples fluorinated at different times and temperatures. This behavior is consistent with F-induced lattice expansions previously reported upon fluorination of bulk $SrMnO_{2.5-x}F_{0.5+x}$ [25] and $Sr(Mn,Fe)O_{3-\delta}F_{\gamma}$ [18,28,42]. The F^- substitution of O^{2-} partially reduces the Mn^{3+} to Mn^{2+}, which increases the average ionic radii of the *B*-site cations [28]. While this previous work has established that the fluorination process removes oxygen from the film, we do not have a means to accurately quantify the decrease in oxygen content (δ) following fluorination although we estimate that each F substitutes for one O. Contrary to the fluorination process, the ozone anneal decreases the *c*-axis parameter to 3.776 Å as expected for the oxidization of Mn^{3+} to Mn^{4+}. This is consistent with the lattice volume decrease in powder $La_{1-x}Sr_xMnO_{3-\delta}$ with decreasing amounts of oxygen vacancies [43]. Our fits to the XRD data confirm the thickness of the as-grown film and the oxyfluoride films to be approximately 100

unit cells, which indicates that despite changes in the lattice constants, fluorination with PTFE does not degrade the film crystallinity at these fluorination conditions.

XRR measurements and fittings are shown in figure 2(c). The film thickness of the as-grown film is 390±3 Å with a root-mean-square roughness (R_{RMS}) of 8.1 Å. After ozone annealing, the film thickness decreased to 371±3 Å, which is consistent with the *c*-axis parameter shrinking. The R_{rms} of the ozone-annealed film is 10.8 Å, revealing that the ozone annealing resulted in slight surface degradation. However, in oxyfluoride $SrMnO_{2.5-\delta}F_{\gamma}$ films, the film thickness is within the range of 390±5 Å. The film thickness obtained from XRR matches well with the thickness used in the XRD simulations, with a less than 5% difference between the two techniques for the fluorinated and as-grown films. The R_{RMS} values of the oxyfluoride films decreased from the as-grown film value (= 8.1 Å) to 8.0, 7.4, and 5.6 Å for 60, 240, and 480 minutes of fluorination. The decreasing of R_{RMS} may be caused by the longer annealing time. A table of the structural parameters obtained from the x-ray analysis for all five samples is presented in table S1 of the supplemental material.

STEM-HAADF images of a fluorinated $SrMnO_{2.5-\delta}F_{0.1}$, an as-grown $SrMnO_{2.5}$, and an ozone treated $SrMnO_3$ film are presented respectively in figures 3(a)-(c). We discern very homogeneous contrast in the $SrMnO_{2.5}$ and $SrMnO_3$ compounds whereas some contrast variations are observed within the fluorinated film. From structural analysis, the *a* and *c* lattice parameters of the as-grown film, the oxygenated film and the fluorinated film are 3.87±0.02 / 3.81±0.02 Å, 3.87±0.02 / 3.80±0.02 Å and 3.87±0.02 Å / 3.83±0.02 Å, respectively. This is in good agreement with the X-ray analysis and is consistent with the films being strained to the substrates.

3.2. Physical properties

Electronic resistivity data are shown in figure 4; all samples are insulators. As seen in figure 4(a), increasing the F content leads to an increase in resistivity, which increases exponentially with decreasing temperature. No signatures of metal-insulator transitions are found in any of the samples. The room temperature resistivity as a function of F content obtained from multiple growths is plotted in figure 4(b). A nearly linear correlation between the room temperature resistivity and the F content is observed. As shown in Ref. [28], the as-grown $SrMnO_{2.5}$ film is reduced after fluorination, resulting in an increase of Mn^{2+} with increasing γ. If we assume that each F donates one additional electron to the Mn-derived e_g band, then the average electronic occupation is $t_{2g}^3 e_g^{1.14}$ in our most heavily fluorinated sample with γ = 0.14. While fluorination increases electronic resistivity, oxidation of $SrMnO_{2.5}$ to $SrMnO_3$ via ozone annealing reduces the room temperature resistivity by a factor of ~20. This increase in conductivity with oxidation is consistent with previous reports from bulk polycrystalline $SrMnO_{3-\delta}$ samples [44]. Also consistent with previous reports of $SrMnO_3$, we find that the oxidized film is an insulator [45,46]. We note that the formation of the corner-connected MnO_6 network realized in the oxidized $SrMnO_3$ through removal of oxygen vacancies could be anticipated to increase orbital overlap between Mn 3*d* and O 2*p* states [47], thus broadening the electronic bandwidth and increasing electronic conductivity.

Figure 4(c) displays the Arrhenius plots of the experimental transport data over temperatures ranging from 140 K to 300 K. Similar to the resistivity values, the activation energies increase systematically with increasing F content and decrease through oxidation to $SrMnO_3$. The obtained activation energy of ~110 meV for $SrMnO_3$ is consistent with previous report of epitaxial $SrMnO_3$ on LSAT (E_A = 160 meV in Ref. [48]) and is larger than the values of 25 and 51 meV reported for polycrystalline $SrMnO_3$ [44,49]. A similar decrease in activation energy with decreasing O vacancies was observed in $La_{0.8}Ca_{0.2}MnO_{3-y}$ as well [50]. The extracted activation energies are given in table 1. The increase in activation energy with increasing F content further indicates the detrimental effect of fluorination on electronic conduction.

To better understand the electronic transport properties of the films, we assessed the results of DFT calculations on their electronic structures utilizing quasi-classical steady state transport theory. Here the resistivity is described based on the number of carriers, relaxation time, and effective mass of electrons as $\rho \equiv \frac{1}{\sigma} = \frac{1}{\tau q^2} \cdot \left(\frac{m_e^*}{n}\right)$, where τ is the relaxation time, q is the charge of the carrier, m_e^* is the effective mass of the electron, and n is the number of carriers. By assuming that manganite compounds surveyed here exhibit equivalent relaxation times τ, we calculated m_e^* from the band structure at the conduction band edge and n from the population of thermally excited carriers from the density of states. This approximation allows us to

compare the transport properties using $\frac{m_e^*}{n}$ as an effective measure of the conductivity of the materials at a finite temperature (table 2).

As noted, figure 4 shows that the experimental resistivity of $SrMnO_{2.5}$ is higher than that of $SrMnO_3$, by more than an order of magnitude, and the resistivity of the manganese oxyfluorides further increases upon fluorination. Our calculated effective masses generally follow this hierarchy, although for higher levels of fluorination there is not necessarily a monotonic increase in the effective mass. For a comparison, the relative resistivity of these materials to $SrMnO_{2.5}$ based on the factor $\frac{m_e^*}{n}$ is given in the third row of table 2. Qualitatively, the decrease in observed resistivity upon oxidizing $SrMnO_{2.5}$ to $SrMnO_3$ is consistent with these DFT results. In contrast, this evaluation yields a lower resistivity for the fluorinated films, which is inconsistent with the experimental data. This discrepancy suggests that there is a significant change in the relaxation time for different manganite systems surveyed in this study. Introducing F anions likely results in "impurity" scattering centers, which increases the resistivity by shortening the relaxation time. We speculate that the reduction in relaxation time could arise from either the inherit disorder introduced by transforming some of the Mn-O-Mn bonds to Mn-F-Mn bonds or by extrinsic effects such as point defects and anion-site disorder introduced through the fluorination reaction. We note that basic measures of crystalline quality from the films, such as the coherence length obtained from x-ray diffraction, the surface roughness from x-ray reflectivity, and the scanning transmission electronic microscopy images, are largely unchanged by the fluorine incorporation, indicating that the increase in resistivity is not due to degradation in long-range crystallinity.

This effect of fluorination on the electronic transport properties is opposite to that observed in other electron-doped manganites. The observation of increasing resistivity despite the increased e_g occupation and presence of mixed Mn^{2+}/Mn^{3+} valence contrasts to $La_{1-x}Ce_xMnO_3$ [12]. There are also studies of Ce-doping in $SrMnO_3$ manganites, which shows increasing conductivity with electron doping and reduction of the Mn valence [12]. Also, it is noteworthy that *A*-site Ce-substitution in $SrMnO_3$ induces a qualitative change in the magnitude and temperature-dependence of the resistivity as a function of the doping level, especially for nominal electron concentrations of 0.1 Mn^{-1} or lower [51-54]. In contrast, the use of F as an electron-dopant is an effective strategy for tuning transport properties as it monotonically increases the resistivity even under doping concentrations of 0.1 Mn^{-1}.

To understand how the magnetic properties are influenced by the valence of Mn and the F incorporation, the magnetic-field-dependent magnetization (M-H) curves of as-grown $SrMnO_{2.5}$, ozone-annealed $SrMnO_3$ and fluorinated $SrMnO_{2.5-\delta}F_\gamma$ ($\gamma = 0.13$) were measured at 10 K with H applied along the [100] film direction, shown in figure 5. A hysteretic curve is observed, indicative of magnetic order within the films, consistent with previously reported magnetic data from $SrMnO_{3-\delta}$ thin films [55-57]. However, the measured magnetization is very small, < 0.10 μ_B Mn^{-1}, which is consistent with the antiferromagnetic nature of bulk $SrMnO_3$ and $SrMnO_{2.5}$ manganites. For all films, the temperature dependence of the magnetization does not contain any significant features indicative of an antiferromagnetic transition; however, local maxima in magnetization are often not observed in ultrathin films due to the small volume of the sample. Despite the small scale of magnetization, perovskite $SrMnO_3$ shows a weak ferromagnetic-like hysteresis with a saturation value of ~0.10 μ_B Mn^{-1} while $SrMnO_{2.5}$ shows nearly linear response under magnetic field within ~0.01 μ_B Mn^{-1} at 3 T. These trends in the saturation magnetization are reproducible with different sample sets (Supplemental figure S5).

We first checked the susceptibility of canting within the antiferromagnetic state in the manganites, which is one possible origin for the measured magnetic response under magnetic field, by performing DFT calculations with noncollinear spin moments. We artificially rotated the magnetic moments from a collinear (antialigned) direction and relaxed the norm of the moments; the resultant energetics reveal that $SrMnO_3$ and $SrMnO_{2.5}$ exhibit similar propensity to a canted antiferromagnetic state as the energy barrier for rotation is small (<1 meV $atom^{-1}$ as shown in Supplemental figure S7). The result differs from the experimental observation suggesting that the magnetic behavior of $SrMnO_3$ and $SrMnO_{2.5}$ arise from different origins.

The magnetic behavior of $SrMnO_{2.5}$ and its fluorinated form follow that of a conventional antiferromagnetic material. As shown from the linear response of $SrMnO_{2.5}$ under an applied magnetic field, the oxygen deficient manganite remains antiferromagnetic in thin film form. When $SrMnO_{2.5}$ is fluorinated, F^- substitutes for O^{2-} and reduces Mn^{3+} to Mn^{2+}, which increases the local magnetic moment. We

also confirmed through DFT calculations in our previous work that such enhanced local magnetic moments yield non-zero net magnetization [28], which induces the weak ferromagnetic behavior.

We attribute the weak net magnetization of $SrMnO_3$ to the presence of oxygen vacancies in the thin film. $SrMnO_3$ is known to exhibit multiferroic behavior in thin film form with oxygen vacancies [58,59], which are more likely to occur under tensile strain as the presence of vacancies reduces nearby Mn atoms. This is consistent with various saturation magnetization (M_s) values of $SrMnO_3$ thin films in other studies [56,57,60], implying that the control of oxygen stoichiometry determines the FM-like behavior. Last, we also note that such small magnetic responses may arise from other effects, such as surface and interfacial discontinuities that can disrupt the long-range antiferromagnetic ordering in thin films or the presence of trace impurities with magnetic moments. In addition, fluorination triggers multiple local structural changes, electron-doping variations, and disrupts the local symmetry. Thus, further studies with fine-control of stoichiometry and strain levels would be required to deterministically identify the origin of the magnetic behavior of these manganite oxyfluoride films.

We next turn to the effect of ozone annealing and fluorination on the optical properties of the as-grown, fluorinated and ozone-annealed films. The absorption coefficient (α), refractive index (n) and extinction coefficient (k), shown in figures 6(a)-(c), were obtained from the WVASE software package using the Lorentz model with four oscillators, more details of which are provided in the Supplemental Material. figure 6(a) shows the absorption coefficient versus photon energy for four films with different treatments. Comparing the as-grown $SrMnO_{2.5}$ and the ozone-annealed $SrMnO_3$ films, the absorption spectra shift to lower photon energy (are red-shifted) after ozone anneal. The center energies of the Lorentz oscillators are listed in table 3; all obtained fittings parameters are provided in table S2 of the Supplemental Materials. The center energies of all four the Lorentz oscillators of the $SrMnO_3$ film are lower compared to the $SrMnO_{2.5}$, confirming that the absorption features red-shift after the ozone anneal. Contrary to the ozone anneal, all the oscillator energies increase after fluorination indicating that the F incorporation leads to a slight blue-shifting of the absorption spectrum. With increasing F content from $\gamma = 0.02$ to 0.08, E_1 increases by ~0.1 eV, while the energy differences between E_2 and E_3 are ~0.01 eV. Therefore, we conclude that the overall impact of fluorination on the optical transitions is a weak blue-shift combined with a small decrease in the absorption coefficient.

To better understand the nature of the optical transitions, DFT calculations were performed. In figure 7, we show the DFT calculated frequency-dependent optical absorption spectra whose peak positions are listed in table 4, and density of states (DOS) where possible optical transitions are shown as horizontal solid lines. The calculated spectra well reproduce the general trends of the experimental spectra, especially the prominent red-shift of the absorption peaks (E_2, E_3, and E_4) upon ozone-annealing, that transforms $SrMnO_{2.5}$ to $SrMnO_3$, and the decrease in absorption coefficient at the peaks of $SrMnO_{2.5}$ with F incorporation. On the other hand, the slight blue-shift of the absorption peak with fluorination found in the experimental spectra is not pronounced in the DFT calculations. The corresponding calculated frequency-dependent extinction coefficients and refractive indices are also provided in Supplemental figure S8, which show good agreement with the experimental spectra.

We identify three important transitions from the occupied O-2p states to the different unoccupied Mn states: Mn-e_g (transition with E_2), Mn-d t_{2g} (E_3) and e_g (E_4) states. Our assignments confirm that the optical absorption processes are caused by interband transitions and enable us to understand the change of optical properties with ozone-annealing and fluorination. The DOS in figure S9 shows broader O-2p bandwidths for $SrMnO_3$ (6.15 eV) compared to $SrMnO_{2.5}$ (5.42 eV), which indicates that ozone annealing broadens the valence band derived from O-2p states. This partly explains the significant red-shift of optical spectral change upon ozone annealing, while the reconstruction of the conduction band also contributes to the optical properties. As additional O^{2-} ions occupy the vacancy sites of $SrMnO_{2.5}$, the square-pyramidal coordination of Mn in $SrMnO_{2.5}$ is transformed to octahedral coordination in $SrMnO_3$, which changes the distribution of the unoccupied Mn-d states that determine the absorption peaks.

When F is incorporated into $SrMnO_{2.5}$, the major calculated absorption peaks are broadened and reduced. While F-2p states are located ~8 eV below Fermi level and do not directly participate in the optical transitions (figure S9), fluorination modifies the optical properties of $SrMnO_{2.5}$ film by altering the O-2p and Mn-d states. As shown in figure 7(b), the sharp peaks in the DOS of $SrMnO_{2.5}$ are broadened with increasing F content which explains the reduced

absorption. Upon fluorination in $SrMnO_{2.5}$, the number of O-2*p* states in the valence band generally decreases without noticeable narrowing of the bandwidth. In addition, fluorine substituting for an oxygen atom disrupts the local orbital symmetry of nearby Mn atoms as the square pyramidal unit becomes heteroleptic. This feature can be seen from the changes to the Mn-*d* orbitals in the conduction bands, with the well-defined sharp peaks of Mn-*d* orbitals in $SrMnO_{2.5}$ being smoothed out upon fluorination. These combined effects of fluorination result in reduced and broadened absorption peaks.

Conclusion

We presented the structural and physical properties of epitaxial perovskite oxyfluoride $SrMnO_{2.5-\delta}F_{\gamma}$ following topotactic fluorination of $SrMnO_{2.5}$ using PTFE as the fluorine source. The F content was systematically controlled by adjusting the fluorination temperature and time. Incorporation of F into the $SrMnO_{2.5}$ film increases electronic resistivity, which we attribute to a shortening of the carrier relaxation time induced by the presence of F. The electron-doping effect with fluorination leads to a weak magnetic hysteresis, while a slight blue-shift of the optical spectra and decrease in absorption coefficient also occurs. These linear optical responses are attributed to a F-induced redistribution of density-of-states within the O 2*p*-derived valence bands and the Mn *d*-derived conduction bands. The overall effect of fluorination on the physical properties is in contrast to fully oxidized $SrMnO_3$ films, which are shown to exhibit a red-shift of optical absorption features and are more conductive compared to $SrMnO_{2.5}$. This work demonstrates that anionic substitution of F for O in manganite films results in systematic and controllable changes to structural, electronic and optical properties.

Acknowledgements

Work at Drexel was supported by the National Science Foundation (NSF), grant number CMMI-1562223. Thin film synthesis utilized deposition instrumentation acquired through an Army Research Office DURIP grant (W911NF-14-1-0493). Y.S and J.M.R. were supported by NSF (Grant No. DMR-1454688). Calculations were performed using the QUEST HPC Facility at Northwestern, the Extreme Science and Engineering Discovery Environment (XSEDE), which is supported by NSF Grant No. ACI-1053575, and the Center for Nanoscale Materials (Carbon Cluster). Use of the Center for Nanoscale Materials, an Office of Science user facility, was supported by the U.S. Department of Energy, Office of Science, Office of Basic Energy Sciences, under Contract No. DE-AC02-06CH11357. J.V. and N. G. acknowledge funding from a GOA project "Solarpaint" of the University of Antwerp. D.J. acknowledges funding from FWO project G093417N from the Flemish fund for scientific research.

References

[1] Tang G, Yu Y, Chen W and Cao Y 2008 *J. Alloys Compd.* **461** 486

[2] von Helmolt R, Wecker J, Holzapfel B, Schultz L and Samwer K 1993 *Phys. Rev. Lett.* **71** 2331

[3] Gong G Q, Canedy C, Xiao G, Sun J Z, Gupta A and Gallagher W J 1995 *Appl. Phys. Lett.* **67** 1783

[4] Urushibara A, Moritomo Y, Arima T, Asamitsu A, Kido G and Tokura Y 1995 *Phys. Rev. B* **51** 14103

[5] Mori S, Chen C and Cheong S 1998 *Phys. Rev. Lett.* **81** 3972

[6] Ahn K, Wu X, Liu K and Chien C 1996 *Phys. Rev. B* **54** 15299

[7] Jonker G 1954 *Physica* **20** 1118

[8] Hemberger J, Krimmel A, Kurz T, Von Nidda H-A K, Ivanov V Y, Mukhin A, Balbashov A and Loidl A 2002 *Phys. Rev. B* **66** 094410

[9] Mandal P and Das S 1997 *Phys. Rev. B* **56** 15073

[10] Mitra C, Hu Z, Raychaudhuri P, Wirth S, Csiszar S, Hsieh H, Lin H-J, Chen C and Tjeng L 2003 *Phys. Rev. B* **67** 092404

[11] Raychaudhuri P, Mitra C, Mann P and Wirth S 2003 *J. Appl. Phys.* **93** 8328

[12] Philip J and Kutty T 1999 *J. Phys.: Condens. Matter* **11** 8537

[13] Kageyama H, Hayashi K, Maeda K, Attfield J P, Hiroi Z, Rondinelli J M and Poeppelmeier K R 2018 *Nat. Commun.* **9** 772

[14] Ai-Mamouri M, Edwards P, Greaves C and Slaski M 1994 *Nature* **369** 382

[15] Slater P, Edwards P, Greaves C, Gameson I, Francesconi M, Hodges J, Ai-Mamouri M and Slaski M 1995 *Physica C: Supercond.* **241** 151

[16] Ar-nikova E, Lubarsky S, Denisenko D, Shpanchenko R, Antipov E and Van Tendeloo G 1995 *Physica C: Supercond.* **253** 259

[17] Francesconi M, Slater P, Hodges J, Greaves C, Edwards P, Ai-Mamouri M and Slaski M 1998 *J. Solid State Chem.* **135** 17

[18] Berry F J, Ren X, Heap R, Slater P and Thomas M F 2005 *Solid State Commun.* **134** 621

[19] Berry F J, Heap R, Helgason Ö, Moore E, Shim S, Slater P and Thomas M 2008 *J. Phys.: Condens. Matter* **20** 215207

[20] Clemens O, Kuhn M and Haberkorn R 2011 *J. Solid State Chem.* **184** 2870

[21] Katayama T, Chikamatsu A, Hirose Y, Takagi R, Kamisaka H, Fukumura T and Hasegawa T 2014 *J. Mater. Chem. C* **2** 5350

[22] Katayama T, Chikamatsu A, Hirose Y, Fukumura T and Hasegawa T 2015 *J. Sol-Gel Sci. Technol.* **73** 527

[23] Tsujimoto Y, Li J J, Yamaura K, Matsushita Y, Katsuya Y, Tanaka M, Shirako Y, Akaogi M and Takayama-Muromachi E 2011 *Chem. Commun.* **47** 3263

[24] Su Y, Tsujimoto Y, Matsushita Y, Yuan Y, He J and Yamaura K 2016 *Inorg. Chem.* **55** 2627

[25] Lobanov M V, Abakumov A M, Sidorova A V, Rozova M G, D'yachenko O G, Antipov E V, Hadermann J and Van Tendeloo G 2002 *Solid State Sci.* **4** 19

[26] Greaves C and Francesconi M G 1998 *Curr. Opin. Solid State Mater. Sci.* **3** 132

[27] Anitha Sukkurji P, Molinari A, Reitz C, Witte R, Kübel C, Chakravadhanula V, Kruk R and Clemens O 2018 *Materials* **11** 1204

[28] Wang J, Shin Y, Arenholz E, Lefler B M, Rondinelli J M and May S J 2018 *Phys. Rev. Mater.* **2** 073407

[29] Björck M and Andersson G 2007 *J. Appl. Crystallogr.* **40** 1174

[30] Gauquelin N, Van den Bos K, Béché A, Krause F, Lobato I, Lazar S, Rosenauer A, Van Aert S and Verbeeck J 2017 *Ultramicroscopy* **181** 178

[31] Nord M, Vullum P E, MacLaren I, Tybell T and Holmestad R 2017 *Adv. Struct. Chem. Imag.* **3** 9

[32] Kresse G and Furthmüller J 1996 *Phys. Rev. B* **54** 11169

[33] Kresse G and Joubert D 1999 *Phys. Rev. B* **59** 1758

[34] Dudarev S, Peng L-M, Savrasov S and Zuo J-M 2000 *Phys. Rev. B* **61** 2506

[35] Perdew J P, Burke K and Ernzerhof M 1996 *Phys. Rev. Lett.* **77** 3865

[36] Blöchl P E 1994 *Phys. Rev. B* **50** 17953

[37] Monkhorst H J and Pack J D 1976 *Phys. Rev. B* **13** 5188

[38] Caignaert V 1997 *J. Magn. Magn. Mater.* **166** 117

[39] Gajdoš M, Hummer K, Kresse G, Furthmüller J and Bechstedt F 2006 *Phys. Rev. B* **73** 045112

[40] Kronig R D L 1926 *J. Opt. Soc. Am.* **12** 547

[41] Kramers H 1927 *Estratto Atti Congr. Int. Fis. Como.* **2, 545**

[42] Moon E J, Xie Y, Laird E D, Keavney D J, Li C Y and May S J 2014 *J. Am. Chem. Soc.* **136** 2224

[43] Abdelmoula N, Guidara K, Cheikh–Rouhou A, Dhahri E and Joubert J 2000 *J. Solid State Chem.* **151** 139

[44] Lee K and Iguchi E 1995 *J. Solid State Chem.* **114** 242

[45] Chmaissem O, Dabrowski B, Kolesnik S, Mais J, Brown D, Kruk R, Prior P, Pyles B and Jorgensen J 2001 *Phys. Rev. B* **64** 134412

[46] Nakamura M, Sawa A, Fujioka J, Kawasaki M and Tokura Y 2010 *Phys. Rev. B* **82** 201101

[47] Kobayashi S, Tokuda Y, Mizoguchi T, Shibata N, Sato Y, Ikuhara Y and Yamamoto T 2010 *J. Appl. Phys.* **108** 124903

[48] May S J, Santos T S, Bhattacharya A 2009 *Phys. Rev. B* **79** 115127

[49] Chiorescu C, Cohn J and Neumeier J 2007 *Phys. Rev. B* **76** 020404

[50] Tanaka J, Umehara M, Tamura S, Tsukioka M and Ehara S 1982 *J. Phys. Soc. Jpn.* **51** 1236

[51] Hashimoto S, Shimura T and Iwahara H 1999 *ECS Proceedings Volumes* **1999** 379

[52] Suzuki T, Sakai H, Taguchi Y and Tokura Y 2012 *J. Electron. Mater.* **41** 1559

[53] Sakai H, Ishiwata S, Okuyama D, Nakao A, Nakao H, Murakami Y, Taguchi Y and Tokura Y 2010 *Phys. Rev. B* **82** 180409

[54] Jeong C, Ryu J, Noh T, Kim Y-N and Lee H 2013 *Adv. Appl. Ceram.* **112** 494

[55] Mandal A K, Panchal G, Choudhary R and Phase D 2018 *AIP Conf. Proc.* **1953** 100035

[56] Bai J, Yang J, Dong W, Zhang Y, Bai W and Tang X 2017 *Thin Solid Films* **644** 57

[57] Wang F, Zhang Y, Bai Y, Liu W, Zhang H, Wang W, Li S, Ma S, Zhao X and Sun J 2016 *Appl. Phys. Lett.* **109** 052403

[58] Aschauer U, Pfenninger R, Selbach S M, Grande T and Spaldin N A 2013 *Phys. Rev. B* **88** 054111

[59] Becher C, Maurel L, Aschauer U, Lilienblum M, Magén C, Meier D, Langenberg E, Trassin M, Blasco J and Krug I P 2015 *Nat. Nanotechnol.* **10** 661

[60] Maurel L, Marcano N, Prokscha T, Langenberg E, Blasco J, Guzmán R, Suter A, Magén C, Morellón L and Ibarra M 2015 *Phys. Rev. B* **92** 024419

Figures

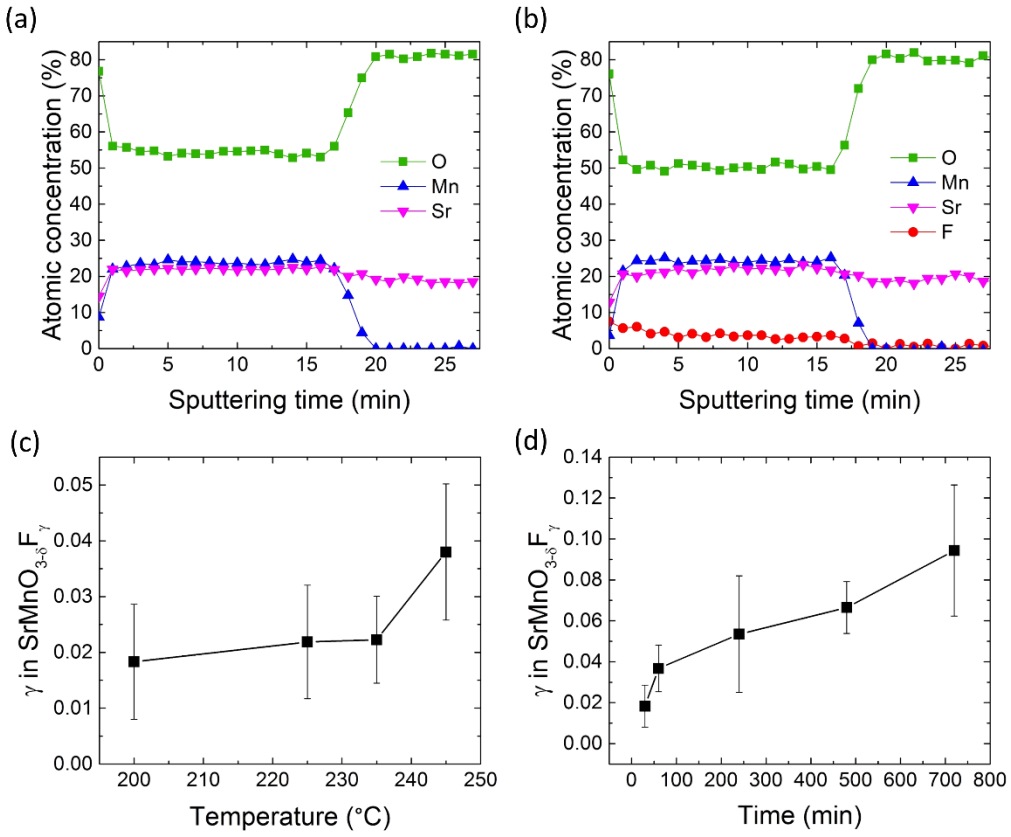

Figure 1. (a) XPS depth profile of as-grown $SrMnO_{2.5}$ films. (b) XPS depth profile of $SrMnO_{2.5-\delta}F_{\gamma}$ oxyfluoride film fluorinated with PTFE at 225 °C for 720 min. (c) F content (γ) as a function of fluorination temperature for 30 min. (d) F content as a function of reaction time at 200 °C. Error bars indicate the standard deviation of the average F concentration throughout the sample obtained from the XPS depth profile.

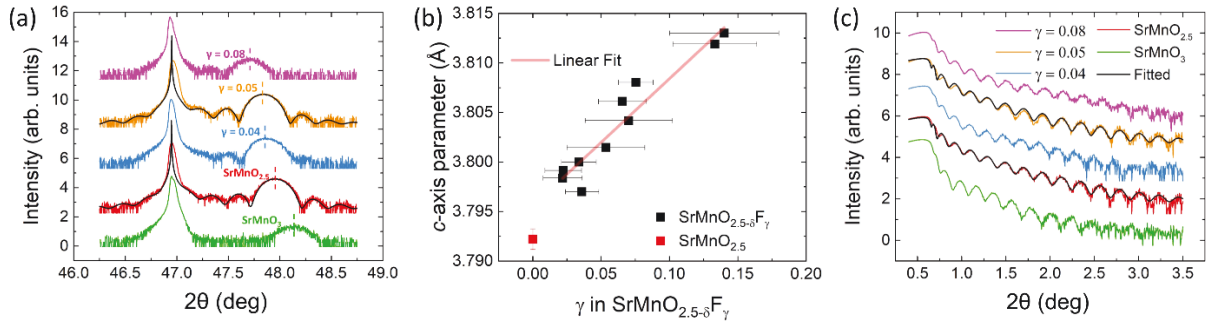

Figure 2. (a) XRD data of as-grown $SrMnO_{2.5}$, ozone annealed $SrMnO_3$ and fluorinated films $SrMnO_{2.5-\delta}F_\gamma$ with different F content. The black lines are the simulations. (b) *c*-axis parameters as a function of F content (γ) in oxyfluoride films. For comparison, the *c*-axis parameter of the oxidized $SrMnO_3$ film is 3.776 Å. The red line is a guide to the eye. (c) XRR data of as-grown, ozone annealed and fluorinated films with different F content. The black lines are the fits obtained from GenX. Data in (a) and (c) are offset for clarity; the y-axes in these plots correspond to the log of intensity, with each tick mark indicating a factor of 10 change in counts.

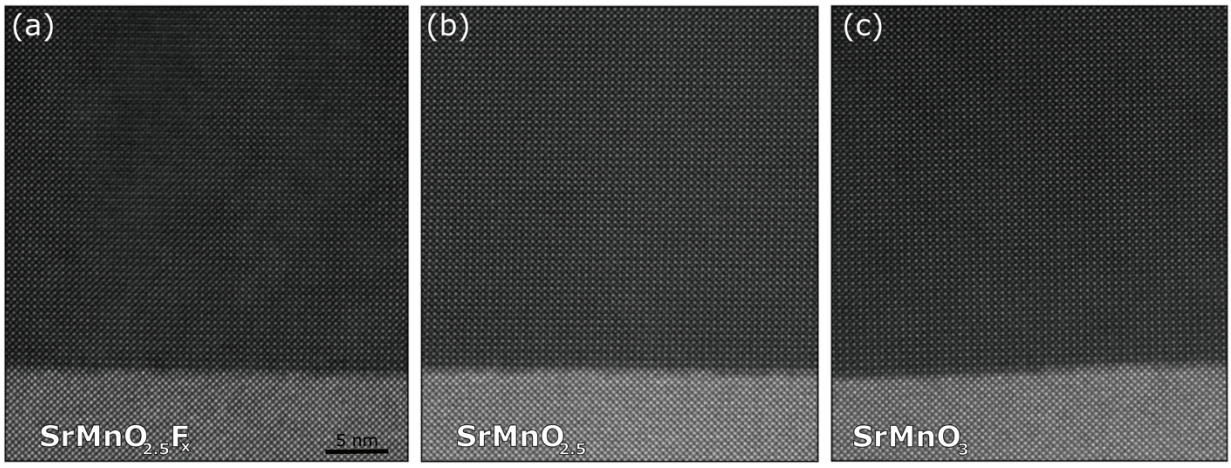

Figure 3. STEM-HAADF images of (a) a fluorinated $SrMnO_{2.5-\delta}F_{0.1}$ film. (b) an as-grown $SrMnO_{2.5}$ film. (c) an ozone treated $SrMnO_3$ film.

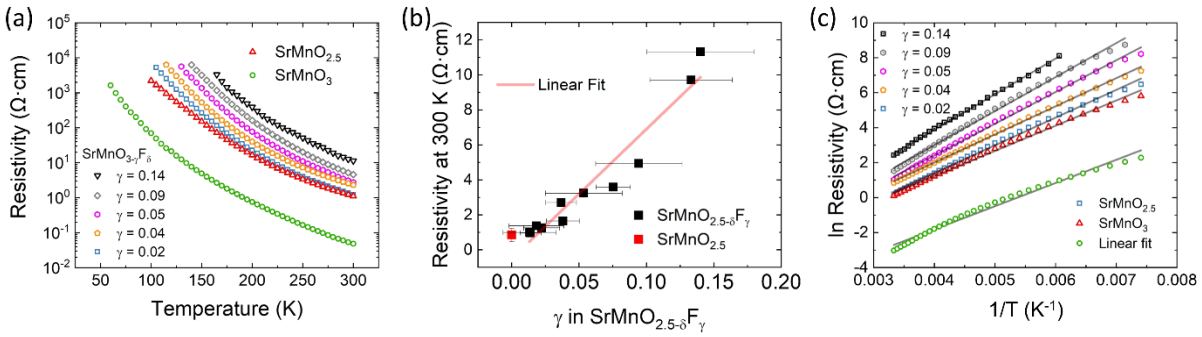

Figure 4. (a) Resistivity as a function of temperature of as-grown $SrMnO_{2.5}$ (red), ozone annealed $SrMnO_3$ (green), and four fluorinated $SrMnO_{2.5-\delta}F_\gamma$ films with $\gamma = 0.02$ (blue), 0.04 (yellow), 0.05 (pink), 0.09 (grey) and 0.14 (black). (b) Room temperature resistivity versus F content. (c) Arrhenius plot showing fitting results to activated behavior over the temperature range of 300 K to 140 K.

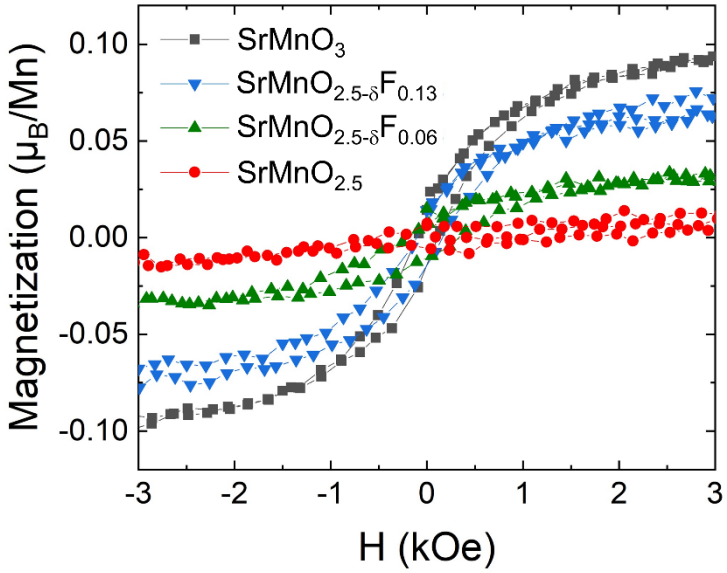

Figure 5. Hysteresis loops of as-grown $SrMnO_{2.5}$, ozone annealed $SrMnO_3$ and fluorinated $SrMnO_{2.5-\delta}F_\gamma$ ($\gamma = 0.06$, and 0.13) films measured at 10 K.

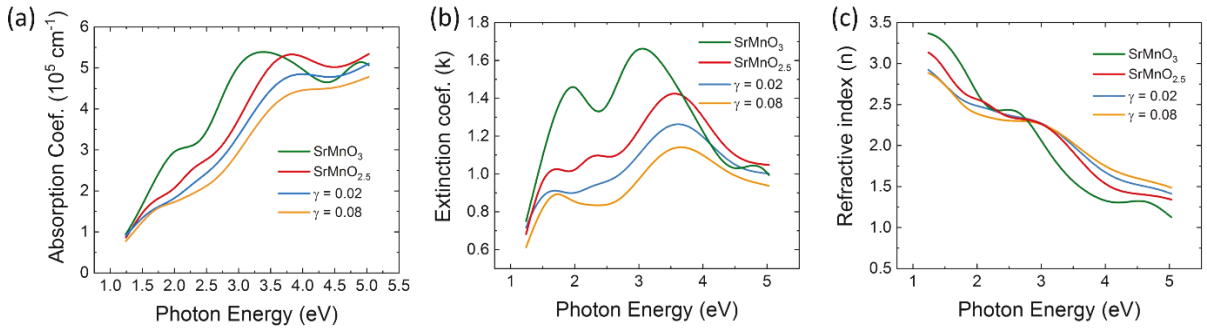

Figure 6. (a) The absorption coefficient, (b) extinction coefficient, and (c) refractive index as a function of photon energy of as-grown (red), ozone-annealed (green), and two fluorinated films with F content γ = 0.02 (blue), 0.08 (yellow).

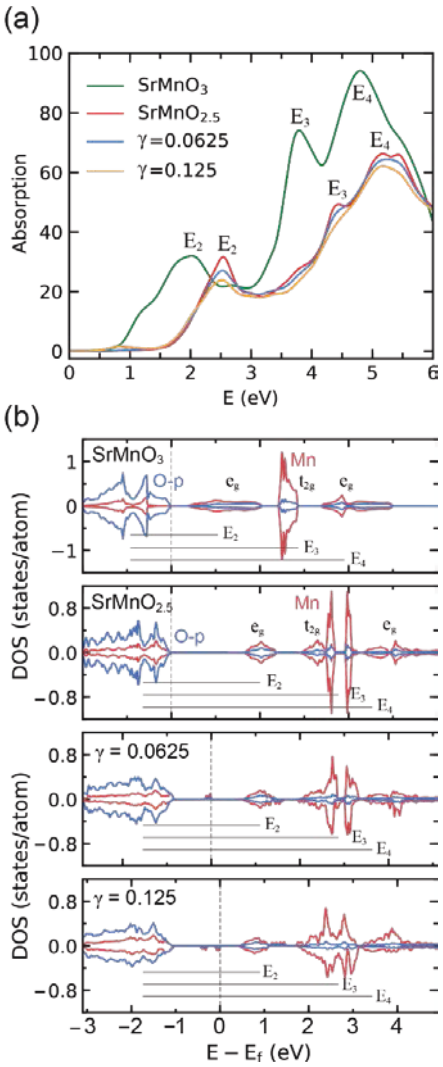

Figure 7. (a) Calculated optical absorption spectra from DFT as a function of photon energy for $SrMnO_3$ (green), $SrMnO_{2.5}$ (red), and two fluorinated manganites $SrMnO_{2.5-\delta}F_\gamma$ with γ = 0.0625 (blue), 0.125 (yellow). (b) Element-resolved density of states (DOS) of each system is given. Horizontal lines represent the energy scales of absorption peaks obtained from DFT.

Tables

Table 1. Activation energies (E_A) obtained from the Arrhenius fits from 140 K to 300 K for $SrMnO_{2.5-\delta}F_\gamma$ and manganite oxides.

	$SrMnO_3$	$SrMnO_{2.5}$	$\gamma = 0.02$	$\gamma = 0.04$	$\gamma = 0.05$	$\gamma = 0.09$	$\gamma = 0.14$
E_A (eV)	0.114	0.124	0.137	0.139	0.157	0.168	0.176

Table 2. Calculated electron effective mass of electron, number of carriers, and relative resistivities of $SrMnO_3$ and $SrMnO_{2.5-\delta}F_\gamma$ are reported using a constant relaxation time and a temperature of 300K.

	$SrMnO_3$	$SrMnO_{2.5}$	$\gamma = 0.0625$	$\gamma = 0.125$
m_e^*/m_e	0.26	0.76	1.09	1.01
n (# electrons cm^{-3})	2.57×10^{24}	8.64×10^{13}	4.82×10^{14}	9.87×10^{14}
m_e^*/n (kg cm^3)	9.20×10^{-56}	8.02×10^{-45}	2.06×10^{-45}	9.32×10^{-46}
ρ / $\rho(SrMnO_{2.5})$ (DFT)	1.15×10^{-11}	1.00	0.257	0.116

Table 3. The results of fitting to the Lorentz model which contains four oscillators. The oscillator center energy E_k are obtained from the fits, where k is the oscillator number. All energy values are given in units of eV.

	Ozone annealed $SrMnO_3$	As-grown $SrMnO_{2.5}$	Fluorinated $SrMnO_{2.5-\delta}F_\gamma$ $\gamma = 0.02$	$\gamma = 0.08$
E_1	1.57	1.57	1.58	1.66
E_2	1.92	2.26	2.30	2.29
E_3	3.00	3.42	3.47	3.46
E_4	4.95	5.17	5.36	6.45

Table 4. The position of peaks in the DFT-calculated absorption spectra. The absorption peaks for E_2, E_3, and E_4 correspond to the experimental oscillator center energies in table 3, while the transition with E_1 is omitted owing to its indefinite position. All energy values are given in units of eV.

	Ozone annealed $SrMnO_3$	As-grown $SrMnO_{2.5}$	Fluorinated $SrMnO_{2.5-\delta}F_\gamma$ $\gamma = 0.0625$	$\gamma = 0.125$
E_2	2.02	2.54	2.53	2.51
E_3	3.76	4.44	4.43	4.42
E_4	4.80	5.18	5.21	5.17